AIAA 2015-0442

SciTech2015
5-9 January, 2015, Kissimmee, FL
53rd AIAA Aerospace Sciences Meeting

Prediction of Wing Flutter Boundary Using High Fidelity Delayed Detached Eddy Simulation

Jia-ye Gan [*], Hong-Sik, Im [†]
Xiang-ying, Chen [‡], Ge-Cheng Zha[§]
Dept. of Mechanical and Aerospace Engineering
University of Miami
Coral Gables, Florida 33124

Crystal L. Pasiliao [¶]
AFRL/RWWV, Munition Aerodynamic Sciences Branch
101 West Eglin Blvd, Suite 330
Eglin AFB FL 32542

Abstract

This paper conducts Delayed Detached Eddy Simulation(DDES) of a 3D wing flutter with free stream Mach number varied from subsonic to supersonic using a fully coupled fluid/structure interaction (FSI). Unsteady 3D compressible Navier-Stokes equations are solved with a system of 5 decoupled structure modal equations in a fully coupled manner. The low diffusion E-CUSP scheme with a 5th order WENO reconstruction for the inviscid flux and a set of 2nd order central differencing for the viscous terms are used to accurately capture the shock wave/turbulent boundary layer interaction of the vibrating wing. The predicted flutter boundaries at different free stream Mach numbers achieve very good agreement with experiment. It appears that the transonic dip phenomenon is due to the anticlimax contribution of the second mode, which is caused by the complicated shock oscillation on the wing.At the flutter boundary including at the sonic dip, no flow separation due to shock/boundary layer interaction is observed.

[*]PhD Student, AIAA Member
[†]PhD., Currently a senior engineer at Honeywell
[‡]PhD., Research Associate Professor
[§]Professor, AIAA Associate Fellow, E-mail: gzha@miami.edu
[¶]PhD., Basic Research Lead

Nomenclature

d	=	distance from the closest wall
f_d	=	delayed LES function in DDES
J	=	Jacobian of the coordinate transformation
I	=	identity matrix
ξ_t, η_t, ζ_t	=	ξ, η, ζ component of grid moving velocity
U, V, W	=	ξ, η, ζ component of contravariant velocity
$U_{i,j}$	=	velocity gradient
x, y, z	=	Cartesian coordinates
δ_{ij}	=	Kronecker delta
Pr	=	Prandtl number
Pr_t	=	turbulent Prandtl number
ν	=	kinematic viscosity
δ_x	=	x-component of displacements of the structure surface
δ_y	=	y-component of displacements of the structure surface
δ_z	=	z-component of displacements of the structure surface
ξ, η, ζ	=	generalized coordinates

Subscripts

i, j, k	=	indices
∞	=	reference variable at free stream

Flutter parameters

b_s	=	wing root semi-chord
$\bar{m}$	=	wing panel mass
$\bar{V}$	=	frustum volume
V^*	=	reduced velocity, $\frac{U_\infty}{b_s \omega_\alpha}$
V_f	=	flutter speed index, $\frac{V^*}{\bar{\mu}}$
ω_α	=	1st torsional mode natural frequency
$\bar{\mu}$	=	mass ratio, $\frac{\bar{m}}{\bar{V}\rho_\infty}$
ω_j	=	natural frequency for jth mode
ζ_j	=	modal damping ratio for jth mode

Abbreviations

$CUSP$	=	convective upwind and split pressure
DES	=	detached eddy simulation
$DDES$	=	delayed detached eddy simulation
FSI	=	fluid/structure interaction
$WENO$	=	weighted essentially non-oscillatory

1 Introduction

Flutter is a self-excited aeroelastic instability which occurs when the aerodynamic damping is negative, and could lead to structural failure. Flutter is a critical problem in aeroelastic design and should be considered in the early phase of aircraft structural design. Experimental testing of aircraft aeroelasticity is very expensive in the design phase. Therefore, tools for aerodynamic flutter prediction are very important to succeed in aircraft design.

Flutter may occur at subsonic and supersonic speed. There are complicated flow phenomena such

as flow separation and shock wave/turbulent boundary layer interaction(STBLI) during flutter. Physical models had been developed to predict the flutter boundary of aircraft. The classical linear models[1] including piston theory and full potential model are widely used in aeroelastic design for the advantage of computational efficiency. The disadvantage of linear modes is that they fail to capture the location and magnitude of local shock motion in transonic and supersonic regime. To predict the transonic or supersonic flutter boundary with higher accuracy, tools based on Euler equations have been developed. Bendiksen et al.[2] study the transonic flutter of typical section wing models by solving the Euler equation coupled with a two degrees of freedom of structural dynamic equations. Reasonably flutter results were obtained in the regions where there are no strong shock. Rausch et al.[3] predict flutter boundary of a set of configuration by solving unsteady Euler aerodynamic equations on unstructured grid. Good agreement was obtained in flutter boundary for subsonic flow. However the predicted flutter characteristics on transonic flow were not satisfactory. Since the the viscous effect on flutter boundary are neglected, neither potential model nor Euler equations are suitable for understanding the STBLI and the mechanism of transonic dip. Prananta et al.[4] reported the results of aeroelastic simulations by using the Euler and the Navier-Stokes solvers. Their calculations show that the viscous effect plays an extremely important role in determining the transonic dip and flutter boundary for a NACA64A010 airfoil. Lee-Rausch et al.[5] also study the effect of viscosity on the flutter boundary of AGARD wing 445.6 by comparing the Euler and Navier-Stokes results over a range of Mach numbers from 0.499 to 1.14. Their calculation shows a significant viscous effect on the supersonic flutter boundary, and the Euler flutter result is quiet different from the Navier-Stokes one on the supersonic side.

Viscous effects can move the shock wave location and the STBLI may induce large separation that change the flutter speed. The drop of transonic flutter boundary is considered due to the presence of part chord shock and its oscillation that is not in phase with the airfoil motion[6]. To understand the mechanism of this non-linear behavior, high fidelity solver based on Navier-Stokes equations coupled with the structural dynamic governing equations is required. Computational methods using Reynolds Averaged Navier Stokes (RANS)[7, 8], large eddy simulation (LES)[9], and direct numerical simulation (DNS)[7, 10] have been utilized to study the STBLI. DNS and LES provide better comparison with experimental results than RANS. Priebe et al[10] employed DNS to study the STBLI on a ramp configuration. They demonstrate that the shock impingement amplifies the pressure fluctuation and there are high-level, low-frequency (< 1000 Hz) vortex structures in the turbulent boundary layer. However, DNS and LES require extremely expensive computational cost. Hence DNS and LES are seldom used in the study the STBLI coupled with the structural vibration. On the other hand, RANS cannot accurately capture the shock oscillation due to the interaction with the turbulent boundary layer without shock unsteadiness correction[9].

The hybrid RANS/LES approach, Detached eddy simulation (DES) suggested by Spalart[11], is developed for complex turbulence problem. DES is designed to take the advantages of RANS and LES methods. In DES, a RANS model is used in the near wall regions to reduce the grid density, and the LES is used outside the near wall regions, which is capable of dealing with massively separated flows. Recently, Chen et al.[12] predict the transonic flutter boundary of AGARD wing 445.6 model by using delayed-detached-eddy simulation(DDES)[11]. In their study, time accurate Navier-Stokes equations are solved with a system of N-decoupled structure modal equations in a fully coupled manner[13, 14]. The computed transonic flutter boundary agrees very well with the experiment. The same method was performed by Im et al.[15] to predict the supersonic flutter boundary of the AGARD wing 445.6 model. Their results appear to be the first time that a numerical prediction of supersonic flutter boundary matches with experiment accurately. The flutter mechanisms in transonic and supersonic condition are not shown in detail in [12, 15]. Furthermore, the complete AGARD wing 445.6 flutter boundary at different Mach numbers from subsonic to supersonic is not provided in their work.

The purpose of this paper is to calculate the full AGARD wing flutter boundary and investigate the flutter mechanism using high fidelity DDES with a fully coupled FSI.

2 Numerical Model for Fluid Flow

2.1 Navier-Stokes Equations

The spatially filtered unsteady compressible Navier-Stokes equations governing the viscous flow over the 3D wing can be written in a normalized form in the generalized coordinates(ξ, η, ζ).

$$\frac{\partial \mathbf{Q}}{\partial t} + \frac{\partial \mathbf{E}}{\partial \xi} + \frac{\partial \mathbf{F}}{\partial \eta} + \frac{\partial \mathbf{G}}{\partial \zeta} = \frac{1}{Re}\left(\frac{\partial \mathbf{E}_v}{\partial \xi} + \frac{\partial \mathbf{F}_v}{\partial \eta} + \frac{\partial \mathbf{G}_v}{\partial \zeta}\right) \tag{1}$$

where Re is the Reynolds number. The equations are non-dimensionalized based on airfoil chord L_∞, free stream density ρ_∞, velocity U_∞, and viscosity μ_∞. The conservative variable vector $\mathbf{Q}$, the inviscid flux vectors $\mathbf{E}$, $\mathbf{F}$, $\mathbf{G}$, and the viscous flux $\mathbf{E_v}$, $\mathbf{F_v}$, $\mathbf{G_v}$ are expressed as

$$\mathbf{Q} = \frac{1}{J}\begin{pmatrix} \bar{\rho} \\ \bar{\rho}\tilde{u} \\ \bar{\rho}\tilde{v} \\ \bar{\rho}\tilde{w} \\ \bar{\rho}\tilde{e} \end{pmatrix}, \mathbf{E} = \begin{pmatrix} \bar{\rho}U \\ \bar{\rho}\tilde{u}U + l_x\bar{p} \\ \bar{\rho}\tilde{v}U + l_y\bar{p} \\ \bar{\rho}\tilde{w}U + l_z\bar{p} \\ (\bar{\rho}\tilde{e} + \bar{p})U - l_t\bar{p} \end{pmatrix}, \mathbf{F} = \begin{pmatrix} \bar{\rho}V \\ \bar{\rho}\tilde{u}V + m_x\bar{p} \\ \bar{\rho}\tilde{v}V + m_y\bar{p} \\ \bar{\rho}\tilde{w}V + m_z\bar{p} \\ (\bar{\rho}\tilde{e} + \bar{p})V - m_t\bar{p} \end{pmatrix}, \mathbf{G} = \begin{pmatrix} \bar{\rho}W \\ \bar{\rho}\tilde{u}W + n_x\bar{p} \\ \bar{\rho}\tilde{v}W + n_y\bar{p} \\ \bar{\rho}\tilde{w}W + n_z\bar{p} \\ (\bar{\rho}\tilde{e} + \bar{p})W - n_t\bar{p} \end{pmatrix} \tag{2}$$

$$\mathbf{E_v} = \begin{pmatrix} 0 \\ l_k\bar{\tau}_{xk} \\ l_k\bar{\tau}_{yk} \\ l_k\bar{\tau}_{zk} \\ l_k(\tilde{u}_i\bar{\tau}_{ki} - \bar{q}_k) \end{pmatrix}, \mathbf{F_v} = \begin{pmatrix} 0 \\ m_k\bar{\tau}u_{xk} \\ m_k\bar{\tau}_{yk} \\ m_k\bar{\tau}u_{zk} \\ m_k(\tilde{u}_i\bar{\tau}_{ki} - \bar{q}_k) \end{pmatrix}, \mathbf{G_v} = \begin{pmatrix} 0 \\ n_k\bar{\tau}_{xk} \\ n_k\bar{\tau}_{yk} \\ n_k\bar{\tau}_{zk} \\ n_k(\tilde{u}_i\bar{\tau}_{ki} - \bar{q}_k) \end{pmatrix} \tag{3}$$

where ρ is the density, p is the static pressure, and e is the total energy per unit mass. The overbar denotes a regular filtered variable, and the tilde is used to denote the Favre filtered variable, ν is kinematic viscosity and $\tilde{\nu}$ is the working variable related to eddy viscosity in S-A model. U, V and W are the contravariant velocities in ξ, η, ζ directions, and are defined as

$$U = l_t + \mathbf{l} \bullet \mathbf{V} = l_t + l_x\tilde{u} + l_y\tilde{v} + l_z\tilde{w} \tag{4}$$

$$V = m_t + \mathbf{m} \bullet \mathbf{V} = m_t + m_x\tilde{u} + m_y\tilde{v} + m_z\tilde{w} \tag{5}$$

$$W = n_t + \mathbf{n} \bullet \mathbf{V} = n_t + n_x\tilde{u} + n_y\tilde{v} + n_z\tilde{w} \tag{6}$$

where J is the Jacobian of the coordinate transformation. l_t, m_t and n_t are the components of the interface contravariant velocity of the control volume in ξ, η and ζ directions respectively. $\mathbf{l}$, $\mathbf{m}$ and $\mathbf{n}$ denote the normal vectors located at the centers of ξ, η and ζ interfaces of the control volume with their magnitudes equal to the surface areas and pointing to the directions of increasing ξ, η and ζ.

$$\mathbf{l} = \frac{\nabla\xi}{J},\ \mathbf{m} = \frac{\nabla\eta}{J},\ \mathbf{n} = \frac{\nabla\zeta}{J} \tag{7}$$

$$l_t = \frac{\xi_t}{J},\ m_t = \frac{\eta_t}{J},\ n_t = \frac{\zeta_t}{J} \tag{8}$$

Let the subscripts i, j, k represent the coordinates x, y, z and use the Einstein summation convention. By introducing the concept of eddy viscosity and sub-grid stress of LES to close the system of equations, the shear stress $\bar{\tau}_{ik}$ and total heat flux $\bar{q}_k$ in Cartesian coordinates can be expressed in tensor form as

$$\bar{\tau}_{ik} = (\mu + \mu_{DES})\left[\left(\frac{\partial\tilde{u}_i}{\partial x_k} + \frac{\partial\tilde{u}_k}{\partial x_i}\right) - \frac{2}{3}\delta_{ik}\frac{\partial\tilde{u}_j}{\partial x_j}\right] \tag{9}$$

$$\bar{q}_k = -\left(\frac{\mu}{Pr} + \frac{\mu_{DES}}{Pr_t}\right)\frac{\partial \tilde{T}}{\partial x_k} \tag{10}$$

where the molecular viscosity $\mu = \mu(\tilde{T})$ is determined by Sutherland's law, and $\mu_{DES}(= \bar{\rho}\tilde{\nu}f_{v1})$ is determined by the DDES of turbulence[11] as explained in the following section. Eq.(9) and (10) are transformed to the generalized coordinate system in computation. The equation of state as a constitutive equation relating density to pressure and temperature is given as follows;

$$\bar{\rho}\tilde{e} = \frac{\bar{p}}{(\gamma-1)} + \frac{1}{2}\bar{\rho}(\tilde{u}^2 + \tilde{v}^2 + \tilde{w}^2) \tag{11}$$

For simplicity, all the bar and tilde in above equations will be dropped in the rest of this paper.

2.2 Delayed Detached Eddy Simulation of Turbulence[11]

In 2006 Spalart et al.[11] suggested an advanced hybrid RANS/LES turbulence, the delayed detached eddy simulation based on the Spalart-Allmaras one equation model[16] which solves a transport equation for the working variable $\tilde{\nu}$. The turbulent eddy viscosity μ_{DES} related to working variable $\tilde{\nu}$ is given by

$$\mu_{DES} = \rho\nu_t = \rho\tilde{\nu}f_{v1} \tag{12}$$

where

$$f_{v1} = \frac{\chi^3}{\chi^3 + c_{v1}^3} \tag{13}$$

$$\chi = \frac{\tilde{\nu}}{\nu} \tag{14}$$

In the SA model, the transport equation for the working variable $\tilde{\nu}$ yields in generalized coordinate system as

$$\begin{aligned}\frac{\partial \frac{1}{J}\rho\tilde{\nu}}{\partial t} + \frac{\partial \rho\tilde{\nu}U}{\partial \xi} + \frac{\partial \rho\tilde{\nu}V}{\partial \eta} + \frac{\partial \rho\tilde{\nu}W}{\partial \zeta} = \frac{1}{Re}\Bigg(&\frac{\partial \frac{\rho}{\sigma}(\nu+\tilde{\nu})(\mathbf{l}\bullet\nabla\tilde{\nu})}{\partial \xi} \\ &+\frac{\partial \frac{\rho}{\sigma}(\nu+\tilde{\nu})(\mathbf{m}\bullet\nabla\tilde{\nu})}{\partial \eta} + \frac{\partial \frac{\rho}{\sigma}(\nu+\tilde{\nu})(\mathbf{n}\bullet\nabla\tilde{\nu})}{\partial \zeta} + \frac{1}{J}S_\nu\Bigg)\end{aligned} \tag{15}$$

where

$$\begin{aligned}S_\nu = \rho c_{b1}(1-f_{t2})\tilde{S}\tilde{\nu} + \tfrac{1}{Re}\Big[&-\rho\left(c_{w1}f_w - \tfrac{c_{b1}}{\kappa^2}f_{t2}\right)\left(\tfrac{\tilde{\nu}}{d}\right)^2 \\ &+\tfrac{\rho}{\sigma}c_{b2}(\nabla\tilde{\nu})^2 - \tfrac{1}{\sigma}(\nu+\tilde{\nu})\nabla\tilde{\nu}\bullet\nabla\rho\Big] + Re\left[\rho f_{t1}(\Delta q)^2\right]\end{aligned} \tag{16}$$

$$\tilde{S} = S + \frac{\tilde{\nu}}{Rek^2d^2}f_{v2} \tag{17}$$

$$f_{v2} = 1 - \frac{\chi}{1+\chi f_{v1}} \tag{18}$$

$$S = \sqrt{2\Omega_{ij}\Omega_{ij}} \tag{19}$$

$$f_w = g\left(\frac{1+c_{w3}^6}{g^6+c_{w3}^6}\right)^{1/6} \tag{20}$$

$$g = r + c_{w2}(r^6 - r) \tag{21}$$

$$r = \frac{\tilde{\nu}}{Re\tilde{S}k^2d^2} \tag{22}$$

$$f_{t2} = c_{t3}exp\left(-c_{t4}\chi^2\right) \tag{23}$$

$$f_{t1} = c_{t1} g_t exp\left[-c_{t2}\frac{\omega_t^2}{\Delta U^2}\left(d^2 + g_t^2 d_t^2\right)\right] \tag{24}$$

$$g_t = min\left(0.1, \frac{\Delta q}{\omega_t \Delta x_t}\right) \tag{25}$$

Where $\Omega_{ij} = \frac{1}{2}\left(\frac{\partial u_i}{\partial x_j} - \frac{\partial u_j}{\partial x_i}\right)$ is the rotation tensor. ω_t is the wall vorticity at the wall boundary layer trip location, d is the distance to the closest wall, d_t is the distance of the field point to the trip location, Δq is the difference of the velocities between the field point and the trip location, Δx_t is the grid spacing along the wall at the trip location. The values of the coefficients by reference[16] are: $c_{b1} = 0.1355, c_{b2} = 0.622, \sigma = \frac{2}{3}, c_{w1} = \frac{c_{b1}}{k^2} + (1 + c_{b2})/\sigma, c_{w2} = 0.3, c_{w3} = 2, k = 0.41, c_{v1} = 7.1, c_{t1} = 1.0, c_{t2} = 2.0, c_{t3} = 1.1, c_{t4} = 2.0$.

To overcome the modeled stress depletion (MSD) and avoid grid induced separation in DES97[17], the DDES suggested by Spalart et al.[11] switches the subgrid scale formulation in S-A model by redefining the distance to the nearest wall $\tilde{d}$ as

$$\tilde{d} = d - f_d max(0, d - C_{DES}\Delta) \tag{26}$$

where

$$f_d = 1 - tanh([8r_d]^3) \tag{27}$$

$$r_d = \frac{\nu_t + \nu}{(U_{i,j}U_{i,j})^{0.5} k^2 d^2 Re} \tag{28}$$

where $U_{i,j}$ is the velocity gradients, k is the Karman constant, and d is the distance to the nearest wall. Within the boundary layer close to walls, $\tilde{d} = d$, and away from the boundary layer, $\tilde{d} = d - f_d max(0, d - C_{DES}\Delta)$ is most of the cases. f_d is designed to be 1 in the LES region, where $r_d \ll 1$, and 0 elsewhere. Unlike DES97, this modification can fully preserve RANS mode inside boundary layer, therefore the attached boundary layers are safe from MSD. This mechanism enables DDES to behave as a RANS model in the near-wall regions, and the LES away from the wall.

2.3 The Low Diffusion E-CUSP Scheme for Inviscid Flux

The Low Diffusion E-CUSP(LDE) Scheme[18, 19] is used to evaluate the inviscid fluxes. The basic idea of the LDE scheme is to split the inviscid flux into the convective flux E^c and the pressure flux E^p based on the upwind characteristics. With an extra equation from the SA model, the splitting is basically the same as the original scheme for the Euler equation. This is an advantage over the Roe scheme[20], for which the eigenvectors need to be derived when any extra equation is added to the governing equations. In generalized coordinate system, the flux $\mathbf{E}$ can be split as the following:

$$\mathbf{E}' = E^c + E^p = \begin{pmatrix} \rho U \\ \rho u U \\ \rho v U \\ \rho w U \\ \rho e U \\ \rho \tilde{\nu} U \end{pmatrix} + \begin{pmatrix} 0 \\ l_x p \\ l_y p \\ l_z p \\ p\overline{U} \\ 0 \end{pmatrix} \tag{29}$$

where, U is the contravariant velocity in ξ direction and is defined as the following:

$$U = l_t + l_x u + l_y v + l_z w \tag{30}$$

$\overline{U}$ is defined as:

$$\overline{U} = l_x u + l_y v + l_z w \tag{31}$$

The convective term, E^c is evaluated by

$$E^c = \rho U \begin{pmatrix} 1 \\ u \\ v \\ w \\ e \\ \tilde{\nu} \end{pmatrix} = \rho U f^c,\ f^c = \begin{pmatrix} 1 \\ u \\ v \\ w \\ e \\ \tilde{\nu} \end{pmatrix} \tag{32}$$

let

$$C = c\left(l_x^2 + l_y^2 + l_z^2\right)^{\frac{1}{2}} \tag{33}$$

where $c = \sqrt{\gamma RT}$ is the speed of sound.

Then the convective flux at interface $i + \frac{1}{2}$ is evaluated as:

$$E^c_{i+\frac{1}{2}} = C_{\frac{1}{2}} \left[\rho_L C^+ f^c_L + \rho_R C^- f^c_R\right] \tag{34}$$

where, the subscripts L and R represent the left and right hand sides of the interface. The Mach number splitting of Edwards[21] is borrowed to determine c^+ and c^- as the following:

$$C_{\frac{1}{2}} = \frac{1}{2}\left(C_L + C_R\right) \tag{35}$$

$$C^+ = \alpha^+_L \left(1 + \beta_L\right) M_L - \beta_L M^+_L - M^+_{\frac{1}{2}} \tag{36}$$

$$C^- = \alpha^-_R \left(1 + \beta_R\right) M_R - \beta_R M^-_R + M^-_{\frac{1}{2}} \tag{37}$$

$$M_L = \frac{U_L}{C_{\frac{1}{2}}},\ M_R = \frac{U_R}{C_{\frac{1}{2}}} \tag{38}$$

$$\alpha_{L,R} = \frac{1}{2}\left[1 \pm sign\left(M_{L,R}\right)\right] \tag{39}$$

$$\beta_{L,R} = -max\left[0, 1 - int\left(|M_{L,R}|\right)\right] \tag{40}$$

$$M^+_{\frac{1}{2}} = M_{\frac{1}{2}} \frac{C_R + C_L \Phi}{C_R + C_L},\ M^-_{\frac{1}{2}} = M_{\frac{1}{2}} \frac{C_L + C_R \Phi^{-1}}{C_R + C_L} \tag{41}$$

$$\Phi = \frac{\left(\rho C^2\right)_R}{\left(\rho C^2\right)_L} \tag{42}$$

$$M_{\frac{1}{2}} = \beta_L \delta^+ M^-_L - \beta_R \delta^- M^+_R \tag{43}$$

$$M^{\pm}_{L,R} = \pm\frac{1}{4}\left(M_{L,R} \pm 1\right)^2 \tag{44}$$

$$\delta^{\pm} = \frac{1}{2}\left\{1 \pm sign\left[\frac{1}{2}\left(M_L + M_R\right)\right]\right\} \tag{45}$$

The pressure flux, E^p is evaluated as the following

$$E^p_{i+\frac{1}{2}} = \begin{pmatrix} 0 \\ \mathcal{P}^+ p\, l_x \\ \mathcal{P}^+ p\, l_y \\ \mathcal{P}^+ p\, l_z \\ \frac{1}{2} p \left[\overline{U} + \overline{C}_{\frac{1}{2}} \right] \\ 0 \end{pmatrix}_L + \begin{pmatrix} 0 \\ \mathcal{P}^- p\, l_x \\ \mathcal{P}^- p\, l_y \\ \mathcal{P}^- p\, l_z \\ \frac{1}{2} p \left[\overline{U} - \overline{C}_{\frac{1}{2}} \right] \\ 0 \end{pmatrix}_R \tag{46}$$

The contravariant speed of sound $\overline{C}$ in the pressure vector is consistent with $\overline{U}$. It is computed based on C as the following,

$$\overline{C} = C - l_t \tag{47}$$

The use of $\overline{U}$ and $\overline{C}$ instead of U and C in the pressure vector is to take into account of the grid speed so that the flux will transit from subsonic to supersonic smoothly. When the grid is stationary, $l_t = 0$, $\overline{C} = C$, $\overline{U} = U$.

The pressure splitting coefficient is:

$$\mathcal{P}^{\pm}_{L,R} = \frac{1}{4} \left(M_{L,R} \pm 1 \right)^2 \left(2 \mp M_L \right) \tag{48}$$

The LDE scheme can capture crisp shock profile and exact contact surface discontinuities as accurately as the Roe scheme[19]. However, it is simpler and more CPU efficient than the Roe scheme due to no matrix operation. In the reference[22], the LDE scheme is shown to be more efficient than the Roe scheme when the S-A one equation turbulence model is coupled.

2.4 The 5th Order WENO Scheme

For reconstruction of the interface flux, $E_{i+\frac{1}{2}} = E(Q_L, Q_R)$, the conservative variables Q_L and Q_R are evaluated by using the 5th order WENO scheme[23, 24]. For example,

$$(Q_L)_{i+\frac{1}{2}} = \omega_0 q_0 + \omega_1 q_1 + \omega_2 q_2 \tag{49}$$

where

$$q_0 = \frac{1}{3} Q_{i-2} - \frac{7}{6} Q_{i-1} + \frac{11}{6} Q_i \tag{50}$$

$$q_1 = -\frac{1}{6} Q_{i-1} + \frac{5}{6} Q_i + \frac{1}{3} Q_{i+1} \tag{51}$$

$$q_2 = \frac{1}{3} Q_i + \frac{5}{6} Q_{i+1} - \frac{1}{6} Q_{i+2} \tag{52}$$

$$\omega_k = \frac{\alpha_k}{\alpha_0 + \ldots + \alpha_{r-1}} \tag{53}$$

$$\alpha_k = \frac{C_k}{\epsilon + IS_k},\ k = 0, \ldots, r-1 \tag{54}$$

$$C_0 = 0.1,\ C_1 = 0.6,\ C_2 = 0.3 \tag{55}$$

$$IS_0 = \frac{13}{12} \left(Q_{i-2} - 2Q_{i-1} + Q_i \right)^2 + \frac{1}{4} \left(Q_{i-2} - 4Q_{i-1} + 3Q_i \right)^2 \tag{56}$$

$$IS_1 = \frac{13}{12} \left(Q_{i-1} - 2Q_i + Q_{i+1} \right)^2 + \frac{1}{4} \left(Q_{i-1} - Q_{i+1} \right)^2 \tag{57}$$

$$IS_2 = \frac{13}{12} \left(Q_i - 2Q_{i+1} + Q_{i+2} \right)^2 + \frac{1}{4} \left(3Q_i - 4Q_{i+1} + Q_{i+2} \right)^2 \tag{58}$$

ϵ is originally introduced to avoid the denominator becoming zero and is supposed to be a very small number. In the reference[25], it is observed that IS_k will oscillate if ϵ is too small and also shift the weights away from the optimal values in the smooth region. The higher the ϵ values, the closer the weights approach the optimal values, C_k, which will give the symmetric evaluation of the interface flux with minimum numerical dissipation. When there are shocks in the flow field, ϵ can not be too large to maintain the sensitivity to shocks. In the reference[25], $\epsilon = 10^{-2}$ is recommended for the transonic flow with shock waves.

2.5 Time Marching Scheme

The time dependent governing equation (1) is solved using dual time stepping method suggested by Jameson[26]. A pseudo temporal term $\frac{\partial Q}{\partial \tau}$ is added to the governing Eq. (1). This term vanishes at the end of each physical time step, and has no influence on the accuracy of the solution. An implicit pseudo time marching scheme using line Gauss-Seidel line relaxation is employed to achieve high convergence rate instead of using the explicit scheme[25]. The pseudo temporal term is discretized with first order Euler scheme. Let m stand for the iteration index within a physical time step, the semi-discretized governing equation can be expressed as

$$\begin{aligned}\left[\left(\frac{1}{\Delta\tau}+\frac{1.5}{\Delta t}\right)I-\left(\frac{\partial R}{\partial \mathbf{Q}}\right)^{n+1,m}\right]\delta\mathbf{Q^{n+1,m+1}}\\ = R^{n+1,m}-\frac{3\mathbf{Q^{n+1,m}}-4\mathbf{Q^{n}}+\mathbf{Q^{n-1}}}{2\Delta t}\end{aligned} \tag{59}$$

where $\Delta\tau$ is the pseudo time step, and R is the net flux of the Navier-Stokes equations discretized in space using the schemes described in section II. C to II. D.

3 Structural Model

3.1 Modal Approach

The equation of motion of an N-DOF(degree of freedom) system with mechanical damping and the aerodynamic loading as the excitation force can be presented in matrix form:

$$[\mathbf{M}]\{\ddot{\mathbf{X}}\}+[\mathbf{C}]\{\dot{\mathbf{X}}\}+[\mathbf{K}]\{\mathbf{X}\}=\{\mathbf{F}\} \tag{60}$$

where, $\mathbf{M}$, $\mathbf{C}$, $\mathbf{K}$ are the mass, structural damping and stiffness matrices. $\mathbf{F}$ is total aerodynamic force acting on the wing surface. Total aerodynamic force can be defined as follows:

$$\mathbf{F}=-\oint P\cdot\hat{n}dA+\oint \tau_{\mathbf{w}}\cdot\hat{t}dA \tag{61}$$

where, $\hat{n}$ is the unit normal vector to the wing surface and $\hat{t}$ is the unit tangent vector to the wing surface. P is the fluid static pressure and $\tau_{\mathbf{w}}$ is the fluid wall shear stress acting on the wing surface. Eq. (11) is used to compute static pressure of the wing surface by setting flow velocity components to zero.

To decouple the equations of motion for the damped systems(60), we use the mass normalized mode shape($\tilde{\phi}$) defined as the normal modes divided by square root of the the generalized mass($\sqrt{\phi^T m\phi}$). Let $\{\mathbf{X}\}=[\tilde{\Phi}]\{\mathbf{q}\}$ and premultiply Eq. (60) by the transpose $[\tilde{\Phi}]^T$.

$$\begin{aligned}[\tilde{\Phi}]^T[\mathbf{M}][\tilde{\Phi}]\{\ddot{\mathbf{q}}\}+[\tilde{\Phi}]^T[\mathbf{C}][\tilde{\Phi}]\{\dot{\mathbf{q}}\}+[\tilde{\Phi}]^T[\mathbf{K}][\tilde{\Phi}]\{\mathbf{q}\}\\ =[\tilde{\Phi}]^T\{\mathbf{F}\}\end{aligned} \tag{62}$$

where $\mathbf{q}$ is the vector of the principal coordinates. Using the orthogonality of the system matrices and assuming damping matrix to be a linear combination of the mass and stiffness matrices, Eq. (62) is then completely decoupled and the jth equation will have the form

$$\ddot{q}_j + 2\zeta_j\omega_j\dot{q}_j + \omega_j^2 q_j = \frac{\tilde{\phi}_j^T}{m_j}\mathbf{F} \tag{63}$$

where $[\tilde{\Phi}]^T = [\tilde{\phi}_1, \cdots, \tilde{\phi}, \cdots, \tilde{\phi}_N]^T$. N is the number of modal coordinates. ω_j and ζ_j are natural frequency and modal damping ratio for mode j. m_j denotes the jth diagonal element of modal mass matrix which will be unity. In the current study, the structural system may be reduced to only five mode shapes, since a few bending and torsional frequencies are usually sufficient to determine flutter. The normalized modal equation can be given as[14]

$$\ddot{q}_j + 2\zeta_j(\tfrac{\omega_j}{\omega_\alpha})\dot{q}_j + (\tfrac{\omega_j}{\omega_\alpha})^2 q_j = \frac{\tilde{\phi}_j^{*T}}{m_j^*} \cdot \mathbf{F}^* \cdot {V_f}^2 \cdot \frac{b_s^2 L}{\bar{V}} \cdot \bar{m} \tag{64}$$

where the dimensionless quantities are denoted by an asterisk. $V_f(= \frac{U_\infty}{b_s\omega_\alpha\sqrt{\bar{\mu}}})$ is the flutter speed index which is an input flutter control parameter. $\bar{m}$ is the measure wing panel mass, $\bar{V}$ represents the conical frustum volume and b_s is the streamwise root semi chord. L is the reference length and ω_α is the angular frequency of the first torsional mode in units $radians/sec$. $\bar{\mu}(= \frac{\bar{m}}{\bar{V}\rho_\infty})$ stands for the mass ratio, i.e. the ratio between the structural mass and the mass of the equivalent volume of fluid at reference density. It is noticed that m_j^* should be equal to one when the mass normalized mode shapes are used. For an example, the mode shapes of AGARD wing 445.6 Weakend model 3 reported by Yates[27] are normalized using the generalized mass such that m_j^* equals one in units $lbf \cdot in \cdot s^2$. This corresponds to 0.112979 $kg \cdot m^2$ in SI units.

The equations are then transformed to a state form as follows:

$$[\mathbf{M}]\frac{\partial \mathbf{S}}{\partial t} + [\mathbf{K}]\{\mathbf{S}\} = \mathbf{q} \tag{65}$$

where

$$\mathbf{S} = \begin{pmatrix} q_j \\ \dot{q}_j \end{pmatrix}, \mathbf{M} = [I], \mathbf{K} = \begin{pmatrix} 0 & -1 \\ (\frac{\omega_j}{\omega_\alpha})^2 & 2\zeta_j(\frac{\omega_j}{\omega_\alpha}) \end{pmatrix}$$

$$\mathbf{q} = \begin{pmatrix} 0 \\ \phi_j^{*T} \cdot \mathbf{F}^* \cdot V_f \cdot \frac{b_s^2 L}{\bar{V}} \cdot \bar{m} \end{pmatrix}$$

3.2 Implicit Structural Solver

To solve the structural equations with CFD solver[18, 19] in a fully coupled manner, the decoupled structural equations are integrated using the same method as the flow governing equations(59) within each physical time step:

$$\begin{aligned} &\left(\tfrac{1}{\Delta\tau}I + \tfrac{1.5}{\Delta t}M + K\right)\delta S^{n+1,m+1} \\ &= q^{n+1,m+1} - M\tfrac{3S^{n+1,m} - 4S^n + S^{n-1}}{2\Delta t} - KS^{n+1,m} \end{aligned} \tag{66}$$

The fluid/structural interaction is implemented in a fully coupled manner[14]. Within each physical time step, the flow equations and structural equations are solved iteratively via every successive pseudo time step until the prescribed convergence criteria is satisfied for both flow and structural solver. After the convergence criteria is reached, the fluid-structural interaction goes to next physical time step.

3.3 Parameters for Flutter Control

There are in general three wing flutter control(or input) parameters: mass ratio $\bar{\mu} = \frac{\bar{m}}{\bar{V}\rho_\infty}$, reduced velocity $V^* = \frac{U_\infty}{b_s\omega_\alpha}$, and flutter speed index $V_f = \frac{V^*}{\bar{\mu}}$. The mass ratio $\bar{\mu}$ takes into account the effect of stiffness in flutter. It represents the ratio between the structural mass and the mass of the equivalent volume of fluid

Table 1: AGARD Wing 44.5 Weakend model 3 [27]

Airfoil section	NACA 65A004
Measured panel mass($\bar{m}$) [kg]	1.8627
Panel span(H) [m]	0.762
Sweep angle at half chord [deg]	43.15
Root chord(b_s) [m]	0.559
Tip chord(b_t) [m]	0.3682
Aspect ratio	1.65

at reference density. Typically flutter speed index V_f is selected as the main parameter in flutter boundary prediction because V_f reflects the effects of both dynamic pressure of the surrounding flow and stiffness of the structure. The effect of aircraft altitude in wind tunnel tests[27, 28] is obtained based on variation of dynamic pressure(varying the density) at constant Mach number. Liu[29] and Chen[14] used V_f, whereas Bakhle[30] used V^* to find the flutter boundary at a given Mach number. In this study, either V_f or V^* can be used explicitly as shown in Eq. (64). The V_f is selected for the wing flutter simulation.

Several iterations are usually needed for a given freestream Mach number to search the neutrally stable point. Most of the computations only need to calculate a few periods to see whether the responses are divergent or damped with time. The flutter velocity index V_f is iterated to find the flutter boundary, all other variables such as inlet total pressure, inlet total temperature, and the static pressure at outlet are not varied. The Reynolds number, $R_e = \frac{\rho_\infty U_\infty L_\infty}{\mu_\infty}$ varies with the freestream velocity. In the wing flutter experiment[28], dynamic pressure $q = \frac{1}{2}\rho_\infty V_\infty^2$ is the main fluid quantity to adjust flutter level. The way to control the dynamic pressure is either by changing the free stream density using the real gas such as freon-12 or by changing the velocity instead of density. In this paper, we change the freestream velocity, U_∞ which has direct relation with the reduced velocity V^*, and hence the flutter velocity index V_f.

4 Boundary Conditions

For the subsonic flutter calculations, steady state freestream conditions are used at the upstream portion of the outer boundary. At downstream boundary, the static pressure is specified as freestream value, and the streamwise gradients of other variables are forced to vanish. In spanwise direction, the periodic boundary condition is used. For the supersonic flutter case, all the variables are extrapolated at downstream boundary. The supersonic inflow condition with specified inlet Mach number is applied at the upstream portion of the outer boundary. The rest of the boundary conditions for the supersonic case are the same as those for the subsonic cases. The wall treatment suggested in [25] to achieve flux conservation by shifting half interval of the mesh on the wall is employed. During the calculation, the Mach number is kept constant by change of Reynolds number with the change of free stream velocity.

5 Computational Model

5.1 The geometry of AGARD wing 445.6

A limited number of AGARD standard wing configurations were tested[27] in order to promote the evaluation of existing and emerging unsteady aerodynamics codes and methods for flutter from subsonic to supersonic regime. In this study, the AGARD Wing 445.6 Weakend 3 is used for flutter simulation. This wing model has the symmetric NACA65A004 airfoil with a 4% thickness, and the wing structural details are listed in table 1.

5.2 Mesh

The O-mesh topology is used as shown in Fig. 1. The outer span boundary away from the wing tip is about 10 span length of the wing. Total 18 partitioned blocks are used for parallel computation. The 1st grid spacing away from the the wing surface is set to yield y^+ less than unity. The far field boundary is located 50 root chords away from the wing.

5.3 Mode shape

First five mass normalized mode shapes in the report[27] are used, which are displayed in Fig. 2. In the plot, the mode shapes are interpolated from structural nodes to fluid nodes by using radial basis function method, so that the grids in the interface between fluid and structure are one to one connected. Among the five modes, the 1st, 3rd and 5th mode are bending mode, and 2nd and 4th mode are torsion mode. As the initial conditions for the structure, 1st mode initial velocity of the structure in the modal coordinates is assumed whereas others including modal displacements are set to zero. The uniform modal damping ratio(ζ) of 0.0 is applied for all flutter computations to isolate the aerodynamic damping. The unsteady flutter computation is started using the initialized flow field obtained by the unsteady CFD simulation without FSI only. The residual in each physical time step is reduced by three orders, which is achieved usually within 30 iterations.

6 Results and Discussion

6.1 Computational Mesh Test

Mesh convergence test is done for Mach number of 1.072. Three mesh sizes were tested; mesh A=129 (around airfoil)$\times$49(normal to the surface)$\times$49(span), mesh B=$137\times90\times60$, mesh C=$289\times64\times77$. When the mesh is changed, the mode shapes corresponding to the surface mesh coordinates are interpolated by a radial basis function interpolation. Fig. 3 shows the modal displacements of mode 1 for different meshes. The flutter velocity index V_f used for mesh test is 0.30. The predicted responses for mode 1 using mesh B are well converged with mesh C. Therefore, mesh C is chosen for flutter simulations in this study.

6.2 Flutter Simulation of AGARD Wing 445.6

The computed flutter velocity index and frequency compared with experimental data at flutter boundary for six free-stream Mach numbers are shown in Fig. 4. Overall, the computed flutter boundaries are in good agreement with the experimental data. In particular, the predicted flutter boundaries at the two supersonic conditions match the experiment accurately. The sonic dip near $M = 1.0$ in the flutter map is very well captured by the computation. In the frequency plot in Fig. 4, the frequency ratio is defined with the ratio of the frequency of the first mode over the first natural torsional frequency during the neutral vibration. Considered the compared results of flutter frequency, the numerical method with DDES overrate the frequency ratio by about 3.0% for Mach number less than 1.141. The discrepency may be due to the zero damping ratio is used for structural vibration.

The predicted modal displacements for Mach number of 0.499, 0.901, 0.960 and 1.072 with different flutter velocity index(V_f) are displayed in Fig. 5, 6, 7 and 8 respectively. Three different responses, including damped, neutral, diverging are shown in the plots on the left, middle, and on the right. Take the transonic dip M=0.96 as an example, at $V_f = 0.2961$, the response decays in time, whereas at $V_f = 0.3021$ the response is divergent. A neutrally stable point, the flutter boundary, is captured at $V_f = 0.2991$. The damped oscillation with $V_f = 0.2961$ is 1.0% below the boundary. It indicates that the present FSI approach has very good accuracy and is sensitive to a small change of the flutter speed index.

The predicted aerodynamic damping coefficients at $M = 1.072$ are plotted in Fig. 9. The aerodynamic damping can be derived from the logarithmic decrement. The structural damping has been set to zero, so

the coefficients are purely the aerodynamic damping. The flutter occurs with negative aerodynamic damping. The damping of the response is plotted as a function the dynamic pressure, which is corresponding to the flutter speed index. The flutter boundary can be determined by a set of test points. The predicted aerodynamic damping shows that the flutter boundary is at P3, which locates between point P2 and P4. And the dynamic pressure at P3 is about 3100 Pa, which is close the experimental value 3166 Pa.

It is noted that the amplitudes of all the second modes(torsional mode) decrease as the Mach number increases as shown the generalized displacement in Fig. 5, 6, 7 and 8. The ratio of the maximum amplitude of the first mode(bending mode) to the second mode versus different free stream Mach numbers at neutral vibration is shown in Fig. 10. It is clear that the weight of the torsional mode that contributes to the flutter of the wing decreases at transonic and supersonic regime. The contribution of the bending mode to structural flutter increases abruptly at transonic Mach number 0.96. It appears that the transonic dip is due to the anticlimax of the second mode in transonic regime.

The force coefficients during neutral vibration at M=0.499, M=0.96 and M=1.072 are shown in Fig. 11. At the flutter boundary, all Cl and Cm show limited oscillation with same period and the phase of Cm is lagged by a half period of oscillation compared to the Cl. Compared to the amplitudes of lift coefficient(Cl) and moment coefficient(Cm), the amplitudes of drag coefficients(Cd) increase from subsonic to supersonic. Particularly, there is an abrupt increment of the amplitude of Cd at transonic condition.

Fig. 12 shows the modal force defined as $\frac{\tilde{\phi}_j^{*T}}{m_j^*} \cdot \mathbf{F}^* \cdot {V_f}^2 \cdot \frac{b_s^2 L}{V} \cdot \bar{m}$ for M=0.499, M=0.96 and M=1.072. In general, the amplitude and phase of the modal force of the second mode are nearly the same as that of the first mode. It is expected that the wing vibrates mainly in the plunging and torsional motion since the first mode is bending and the second mode is torsion. Similar to the variation Cd as shown Fig. 11, the amplitude of the second modal force at transonic dip is slightly greater than that of the first mode and the phase slightly lags behind the first mode.

Fig. 13 illustrates the wing tip physical displacement during half a period at the neutral vibration at M=0.96 and M=1.072. It can be seen that both of motions have the same behavior. The amplitude of the trailing edge is larger than that of the leading edge, which indicates that both the pitching and the plunging are associated with the wing flutter. The wing with the pitching (or torsion) experiences a variation of angle of attack(AOA) with time.

The instantaneous Mach number(M_{is}) contours on the suction surface at 4 different Mach numbers at three instants during half a period are shown in Fig. 14 and Fig. 15. M_{is} reflects both the local static pressure and the main flow speed. At subsonic Mach number 0.49, the distribution of M_{is} on the wing surface smooth. At M=0.96, M_{is} contours on the wing surface show a complicated shock wave system. There appears two shock wave systems, one near the root of the wing, and the other starting from wing tip. The strength of shock waves on the wing surface varies during the vibration. As the wing deforms, the two shocks move along the wing span and possibly interact with each other over part of the cycle. The supersonic regions expand and shrink, and possibly disappear at the mid span. At supersonic conditions, M=1.072 and M=1.141, the distribution of shock wave becomes simpler. The shock wave is located near the trailing edge and starts from the wing tip and disappears near the root of the wing. The shock wave appearance near the trailing edge may be responsible for the torsion mode amplitude depletion in the transonic and supersonic regime shown in Fig. 10.

Fig. 16 shows M_{is} profiles at different span locations and time instants during the supersonic flutter. The unsteady shock waves near the trailing edge of the wing is well captured by current method. It can be seen that small lifts are generated near the tip span due to the variation of the AOA during the wing vibration. It appears that the structural deformations also affects the location and strength of the part-chord shock to a significant degree, which in turn results in a shift in the aeroelastic stability of the wing. The shocks is thus capable of turning bending-torsion flutter instability into bending flutter.

Fig. 17 shows the Mach number contours at three time instants at three different span locations at near root, mid-span, and near tip with M=0.96. The shock is relatively more stable near root and largely oscillates near the tip. At the flutter boundary including at the sonic dip, no flow separation due to

shock/boundary layer interaction is observed.

7 Conclusion

In this paper, DDES of a 3D wing flutter is conducted with free stream Mach number varied from subsonic to supersonic. Unsteady 3D compressible Navier-Stokes equations are solved with a system of 5 decoupled structure modal equations in a fully coupled manner. The low diffusion E-CUSP scheme with a 5th order WENO reconstruction for the inviscid flux and a set of 2nd order central differencing for the viscous terms are used to accurately capture the shock wave/turbulent boundary layer interaction of the vibrating wing. The radial basis function is employed to interpolate the mode shapes from the coarse mesh to refined mesh.

The predicted flutter boundary at different free stream Mach number achieves very good agreement with experiment. In particular, the predicted flutter boundaries at the two supersonic conditions match the experiment accurately.

The weight of the torsional mode that contribute to the flutter of the wing decrease at transonic and supersonic regime. The contribution of the bending mode to structural flutter increase abruptly at transonic Mach number 0.96. It appears that the transonic dip is due to the anticlimax of the second mode in transonic regime.

There are complicated shock wave systems along the wing span in transonic regime. The strength of shock wave on the wing surface varies during the vibration. As the wing deforms in response to unsteady loads, the supersonic regions grow and shrink in harmony with the wing motion. The abrupt change of amplitude of Cd, modal displacement and force may be due to the complicated wave systems at transonic condition.

Acknowledgments

The simulation was performed under the support of High Performance Computing Challenge Project of DoD Supercomputing Resource Centers and the Center for Computational Sciences at University of Miami.

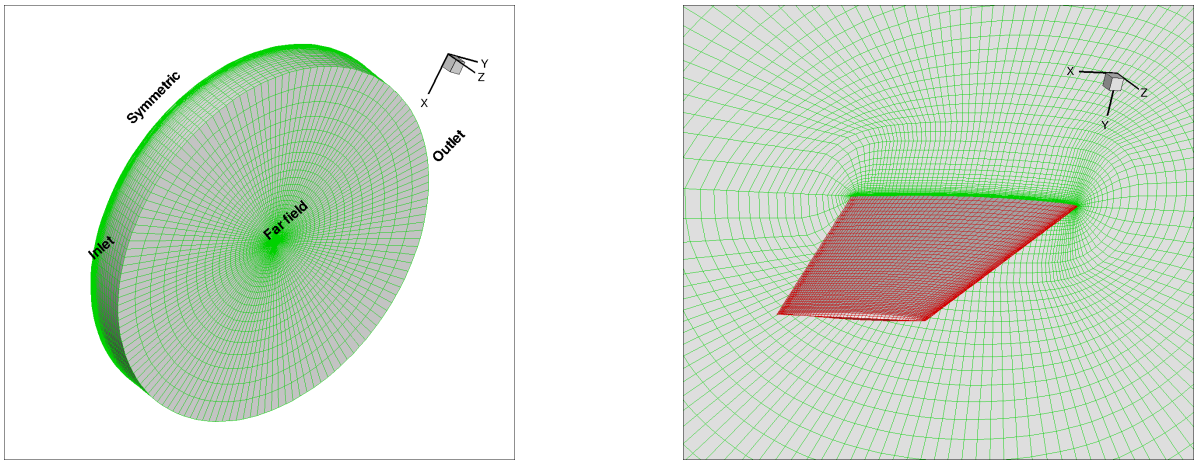

Figure 1: Computational mesh of 289×64×77 for AGARD Wing 445.6 Weakend 3

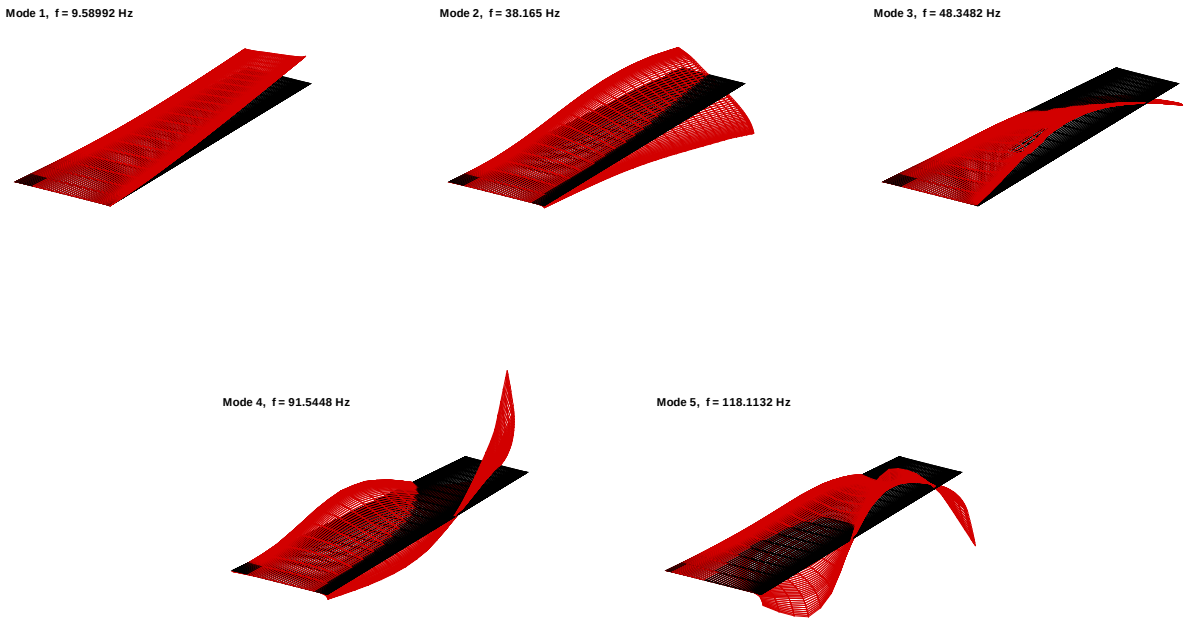

Figure 2: The first 5 mode shapes of AGARD Wing 445.6 Weakend 3[27]

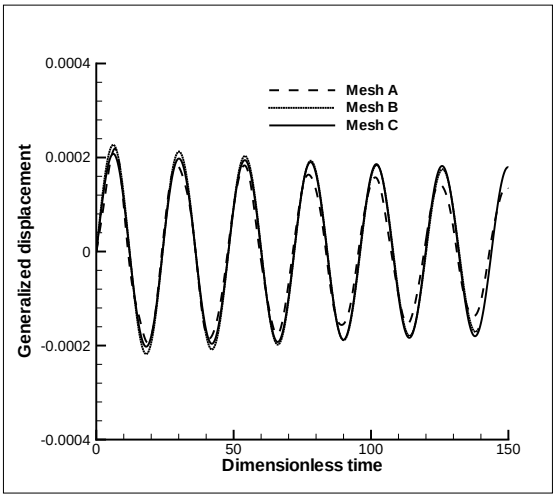

Figure 3: Mesh convergence test for $M = 1.072$, $V_f = 0.30$

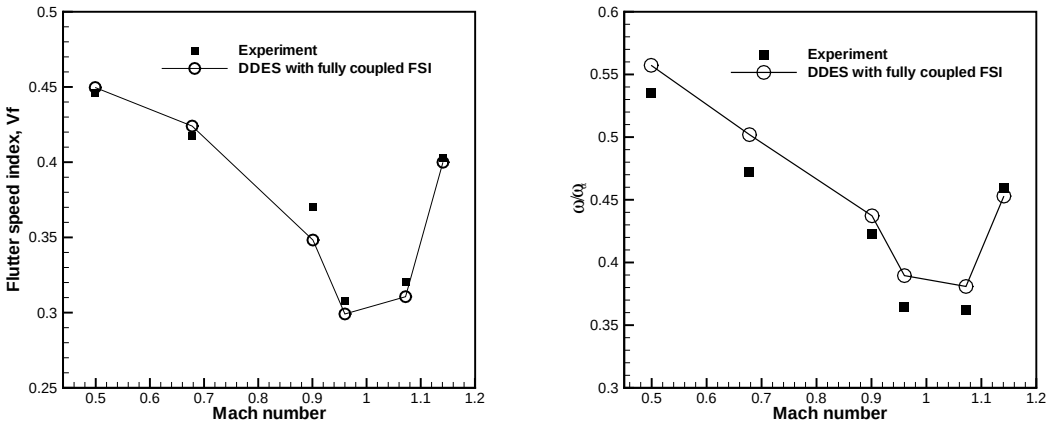

Figure 4: Flutter boundary predicted by fully coupled FSI methods and DDES for Wing 445.6

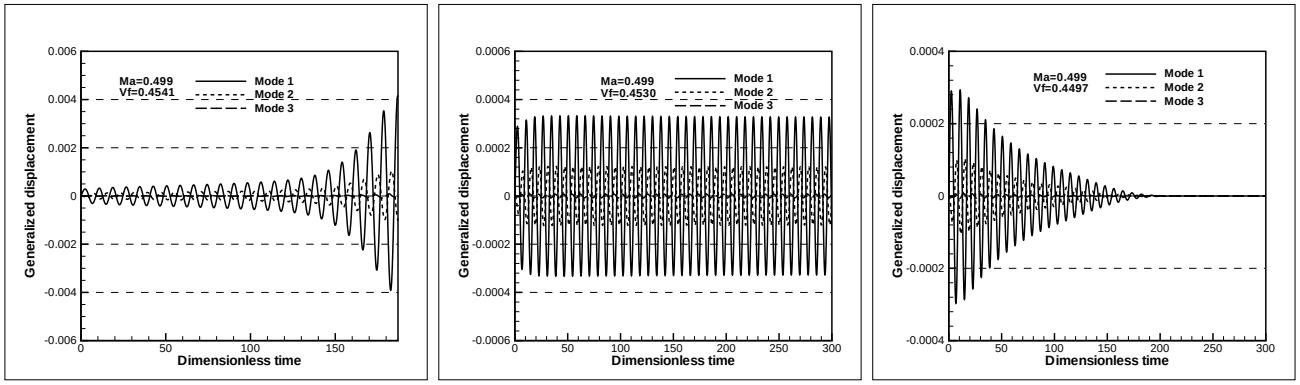

Figure 5: Modal displacements for $M = 0.499$

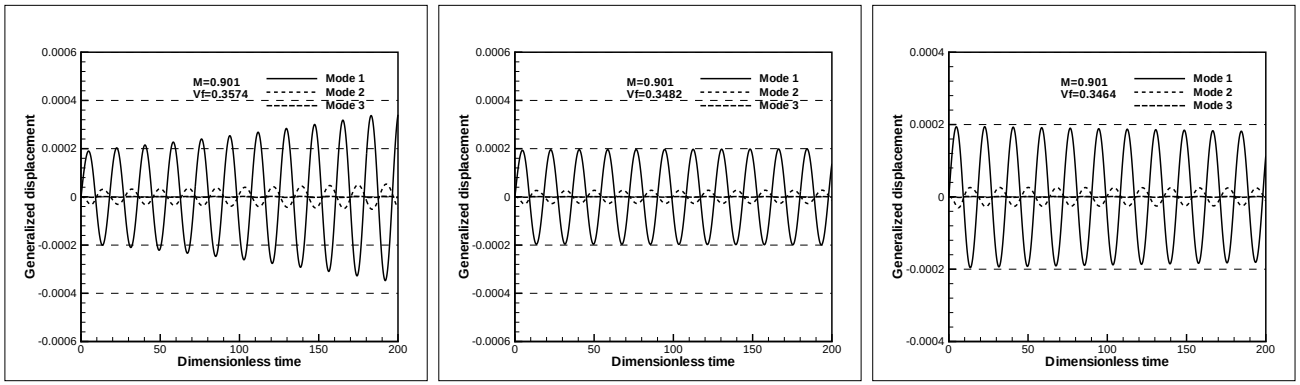

Figure 6: Modal displacements for $M = 0.901$

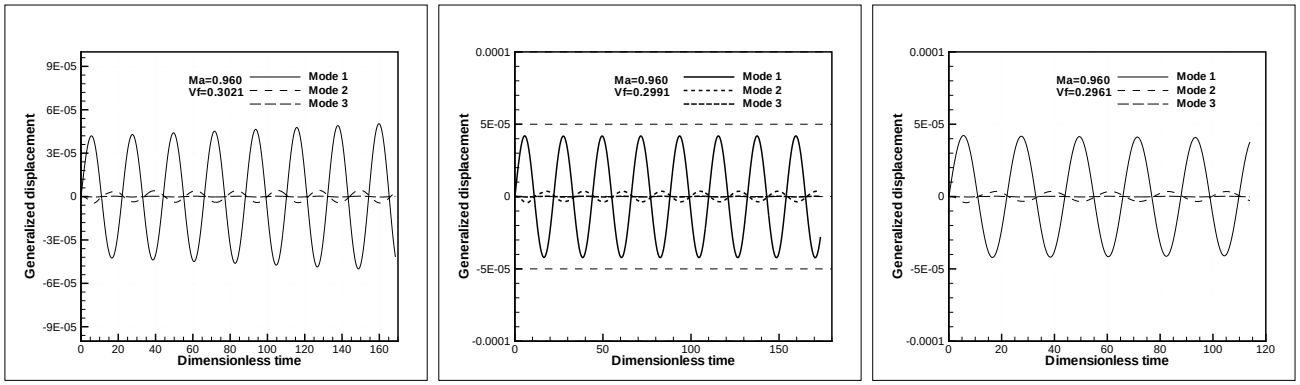

Figure 7: Modal displacements $M = 0.960$

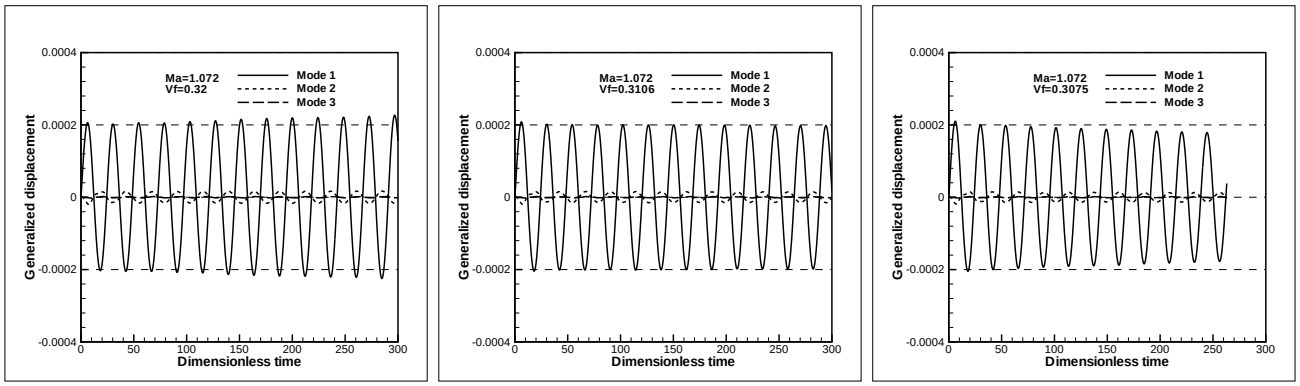

Figure 8: Modal displacements for $M = 1.072$

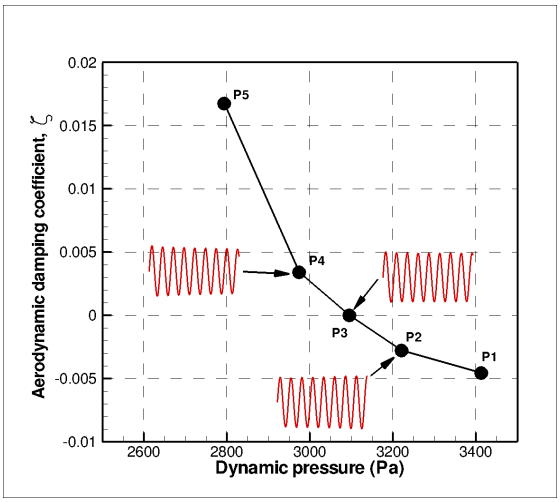

Figure 9: Aerodynamic damping as a function of the dynamic pressure for $M = 1.072$

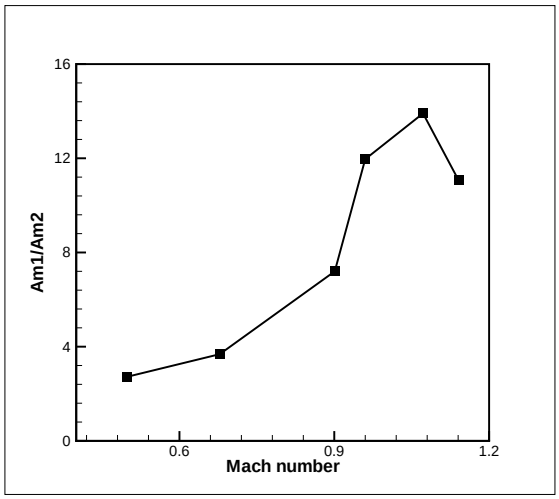

Figure 10: Maximum amplitude ratio of the first mode over the second mode

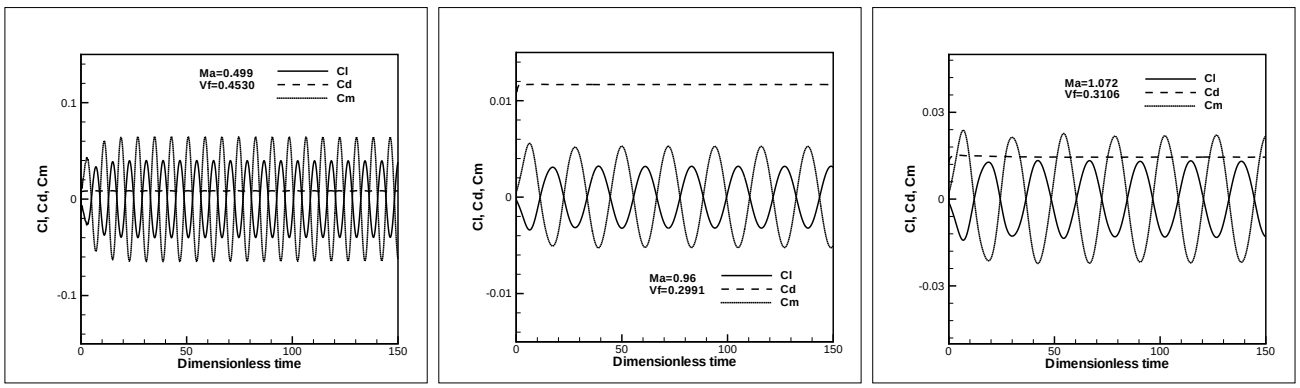

Figure 11: Comparison of predicted lift(C_l),drag(C_d), and momentum coefficients during neutral vibration at different Mach numbers

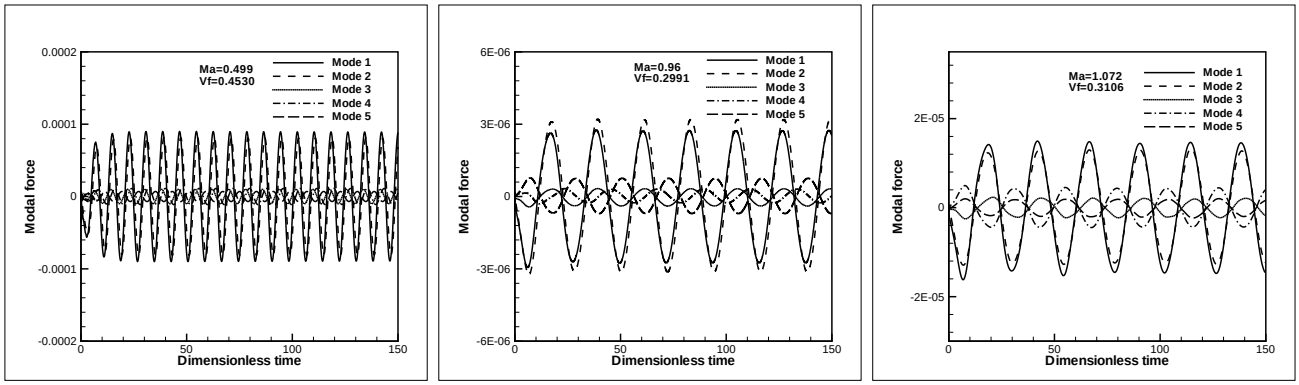

Figure 12: Comparison of modal force ($\frac{\tilde{\phi}_j^{*T}}{m_j^*} \cdot \mathbf{F}^* \cdot {V_f}^2 \cdot \frac{b_s^2 L}{V} \cdot \bar{m}$) during neutral vibration at different Mach numbers

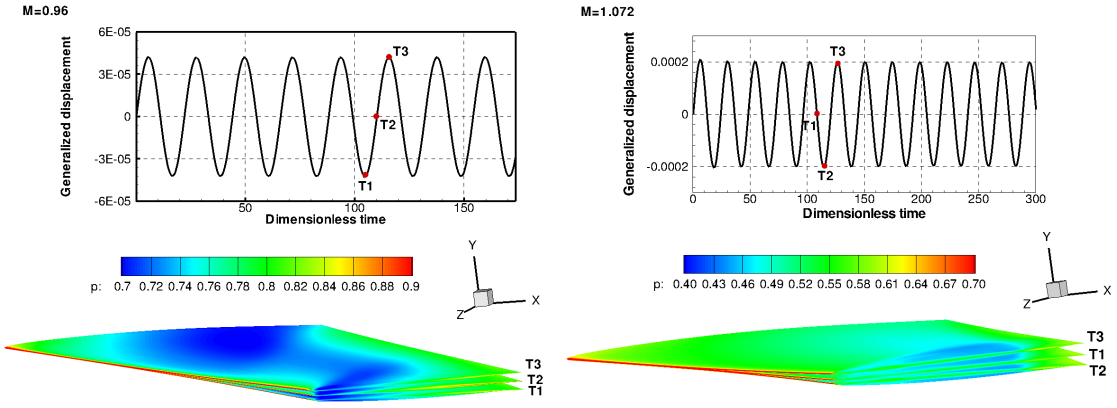

Figure 13: Wing fluttering at $M = 0.96$ and $M = 1.072$ during neutral vibration

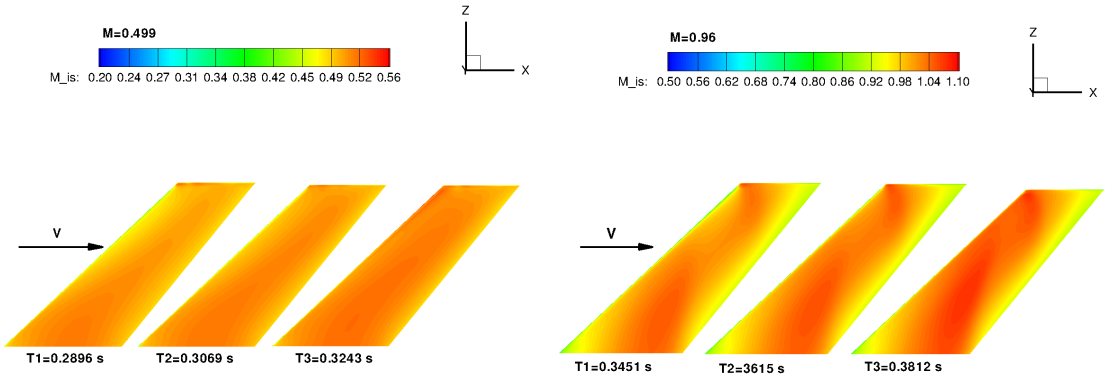

Figure 14: Instantaneous isentropic Mach number contours on suction surface. Left: $M = 0.49$; Right: $M = 0.96$

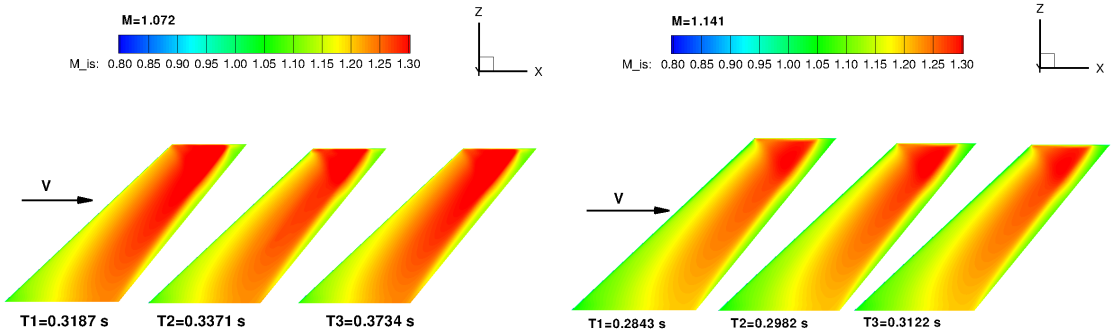

Figure 15: Instantaneous isentropic Mach number contours on suction surface. Left: $M = 1.072$; Right:$M = 1.141$

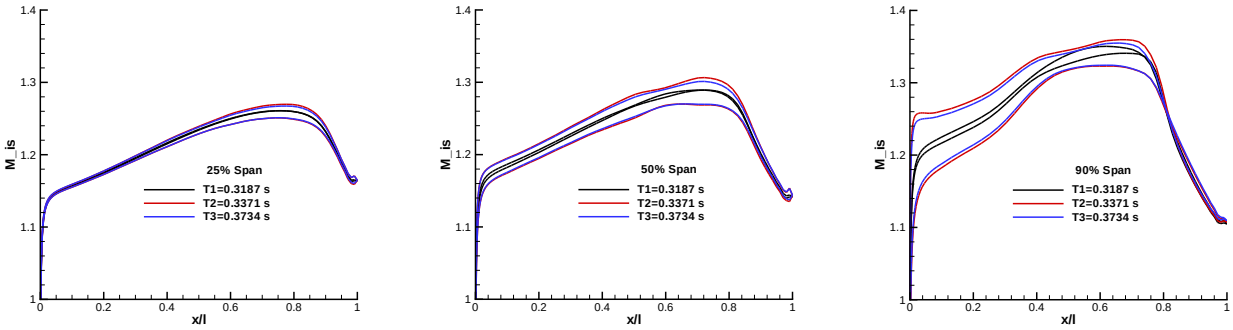

Figure 16: Isentropic Mach number profile for $M = 1.072$

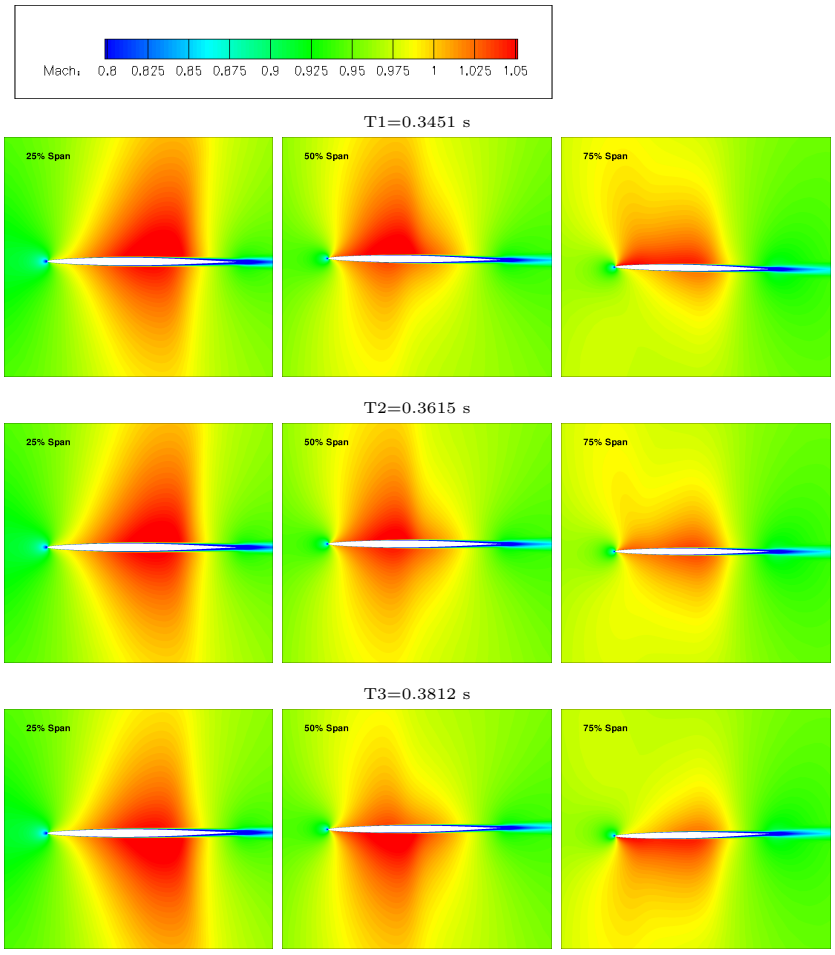

Figure 17: Mach number contours for $M = 0.96$

References

[1] E. H. Dowell, and K. C. Hall, "MODELING OF FLUID-STRUCTURE INTERACTION," *Annual Review of Fluid Mechanics*, vol. 33, pp. 445–490, 2001.

[2] O. Bendiksen and K. Kousen, "Transonic Flutter Analysis Using the Euler Equations." AIAA Paper 87-0911, 1987.

[3] J. Rausch, R.D. Batina and T. Yang, "Three-dimensional time-marching aeroelastic analyses using an unstructured-grid euler method," *AIAA Journal*, vol. 33, pp. 1626–1633, 1993.

[4] B. B. Prananta, H. M. H. L., and Z. R. J., "Two-Dimensional Transonic Aeroelastic Analysis Using Thin-Layer Navier-Stokes Method," *Journal of Fluid and Structures*, vol. 12, pp. 655–676, 1998.

[5] E. Lee-Rausch and J. Batina, "Calculation of AGARD Wing 445.6 Flutter Using Navier-Stokes Aerodynamics." AIAA Paper 93-3476, 1993.

[6] K. Isogai, "Transonic Dip Mechanism of Flutter of a Sweptback Wing: Part II," *AIAA Journal*, vol. 19, pp. 1240–1242, September 1981.

[7] Knight, D., Yan, H., Panaras, A. G., Zheltovodov, A., "Advances in CFD Prediction of Shock Wave Turbulent Boundary Layer Interactions," *Progress in Aerospace Sciences*, vol. 39, pp. 121–184, 2003.

[8] Sinha, K., Mahesh, K., Candler, G., "Modeling the Effect of Shock Unsteadiness in Shock/Turbulent Boundary-Layer Interactions," *AIAA Journal*, vol. 43, pp. 586–594, 2005.

[9] Morgan, B., Kawai, S., Lele, S. K., "Large-Eddy Simulation of an Oblique Shock Impinging on a Turbulent Boundary Layer." AIAA Paper 2010-4467, 40th Fluid Dynamics Conference and Exhibit, June 28 - July 1, Chicago, Illinois, 2010.

[10] S. Priebe, M. Martin, "Direct Numerical Simulation of Shockwave and Turbulent Boundary Layer Interactions." AIAA-2009-0589, 47th AIAA Aerospace Sciences Meeting, January 5-8, Orlando, FL, USA, 2009.

[11] P.R. Spalart, S. Deck, M. Shur, and K.D. Squires, "A New Version of Detached-Eddy Simulation, Resistant to Ambiguous Grid Densities," *Theoritical and Computational Fluid Dynamics*, vol. 20, pp. 181–195, 2006.

[12] X.Y. Chen, B.Y. Wang, and G.C. Zha, "Delayed Detached Eddy Simulation of 3-D Wing Flutter with Fully Coupled Fluid-Structural Interaction." AIAA Paper 2010-0053, 48th AIAA Aerospace Sciences Meeting Including the New Horizons Forum and Aerospace Exposition, Jan. 4-7, 2010.

[13] X.Y. Chen, and G.-C. Zha, "Fully Coupled Fluid-Structural Interactions Using an Efficient High Solution Upwind Scheme," *Journal of Fluid and Structure*, vol. 20, pp. 1105–1125, 2005.

[14] X.-Y. Chen, G.-C. Zha, and M.-T. Yang, "Numerical Simulation of 3-D Wing Flutter with Fully Coupled Fluid-Structural Interaction," *Journal of Computers and Fluids*, vol. 35, pp. 856–867, 2007.

[15] Im, H.-S. and Zha, G.-C., "Prediction of a Supersonic Wing Flutter Boundary Using a High Fidelity Detached Eddy Simulation." AIAA Paper 2012-0039, 50th AIAA Aerospace Sciences Meeting, Jan. 9-12., Nashville, TN, USA, 2012.

[16] P.R. Spalart, and S.R. Allmaras, "A One-equation Turbulence Model for Aerodynamic Flows." AIAA-92-0439, 1992.

[17] P.R. Spalart, W.H. Jou, M. Strelets, and S.R. Allmaras, "Comments on the Feasibility of LES for Wings, and on a Hybrid RANS/LES Approach." Advances in DNS/LES, 1st AFOSR Int. Conf. on DNS/LES, Greyden Press, Columbus, H., Aug. 4-8, 1997.

[18] G.C. Zha, Y.Q. Shen, and B.Y. Wang, "An improved low diffusion E-CUSP upwind scheme ," *Journal of Computer and Fluids*, to appear 2011.

[19] G.C. Zha, Y.Q. Shen, and B.Y. Wang, "Calculation of Transonic Flows Using WENO Method with a Low Diffusion E-CUSP Upwind Scheme." AIAA Paper 2008-0745, 46th AIAA Aerospace Sciences Meeting, Reno, NV, Jan. 2008.

[20] P. Roe, "Approximate Riemann Solvers, Parameter Vectors, and Difference Schemes," *Journal of Computational Physics*, vol. 43, pp. 357–372, 1981.

[21] J. Edwards, "A Low-Diffusion Flux-Splitting Scheme for Navier-Stokes Calculations," *Computer & Fluids*, vol. 6, pp. 635–659, 1997.

[22] B.Y. Wang, and G.C. Zha, "Comparison of a Low Diffusion E-CUSP and the Roe Scheme for RANS Calculation." AIAA Paper 2008-0596, 46th AIAA Aerospace Sciences Meeting and Exhibit, Jan. 7-10, 2008.

[23] Shen, Y.Q., and Zha, G.C., "Improvement of the WENO Scheme Smoothness Estimator," *International Journal for Numerical Methods in Fluids*, vol. 64,, pp. 653–675, DOI:10.1002/fld.2186, 2009.

[24] Shen, Y.Q., Zha, G.C., and Wang, B.Y., "Improvement of Stability and Accuracy of Implicit WENO Scheme," *AIAA Journal*, vol. 47, pp. 331–334, DOI:10.2514/1.37697, 2009.

[25] Y.Q. Shen, B.Y. Wang, and G.C. Zha, "Implicit WENO Scheme and High Order Viscous Formulas for Compressible Flows ." AIAA Paper 2007-4431, 2007.

[26] A. Jameson, "Time Dependent Calculations Using Multigrid with Applications to Unsteady Flows Past Airfoils and Wings." AIAA Paper 91-1596, 1991.

[27] E.C. Yates Jr., "AGARD standard aeroelastic configurations for dynamic response. Candidate configuration I.-wing 445.6 ." NASA-TM-1000492, 1987.

[28] R.V. Goggett, R.V. Rainey, and H.G. Morgan, "An experimental investigsation of Aerodynamic Effects of Airfoil Thickness on Transonic Flutter Characteristics." NASA TMX-79, 1959.

[29] F. Liu, J. Cai, and Y. Zhu, "Calculation of Wing flutter by a Coupled CFD-CSD method." AIAA-2000-0907, 2000.

[30] M.A. Bakhle, T.S.R. Reddy, and T.G. Keith Jr., "Time Domain Flutter Analysis of Cascades Using a Full-Potnetial Solver," *AIAA Journal*, vol. 30, pp. 163–169, 1992.